



### **Science Arts & Métiers (SAM)**

is an open access repository that collects the work of Arts et Métiers Institute of Technology researchers and makes it freely available over the web where possible.

This is an author-deposited version published in: <https://sam.ensam.eu>  
Handle ID: <http://hdl.handle.net/10985/14017>

#### **To cite this version :**

Boudjemaa BOUAOUINA, Cédric MASTAIL, Rubenson MAREUS, Florin NITA, Anny MICHEL, Grégory ABADIAS, Aurélien BESNARD - Nanocolumnar TiN thin film growth by oblique angle sputter-deposition: Experiments vs. simulations - Materials and Design - Vol. 160, p.338-349 - 2018

Any correspondence concerning this service should be sent to the repository

Administrator : [scienceouverte@ensam.eu](mailto:scienceouverte@ensam.eu)





### **Science Arts & Métiers (SAM)**

is an open access repository that collects the work of Arts et Métiers ParisTech researchers and makes it freely available over the web where possible.

This is an author-deposited version published in: <https://sam.ensam.eu>  
Handle ID: <http://hdl.handle.net/null>

#### **To cite this version :**

Boudjemaa BOUAQUINA, Cédric MASTAIL, Aurélien BESNARD, Rubenson MAREUS, Florin NITA, Anny MICHEL, Grégory ABADIAS - Nanocolumnar TiN thin film growth by oblique angle sputter-deposition: Experiments vs. simulations - Materials and Design - Vol. 160, p.338-349 - 2018

# Nanocolumnar TiN thin film growth by oblique angle sputter-deposition: Experiments vs. simulations

Boudjemaa Bouaouina<sup>a,b</sup>, Cédric Mastail<sup>a</sup>, Aurélien Besnard<sup>c</sup>, Rubenson Mareus<sup>a</sup>, Florin Nita<sup>a</sup>, Anny Michel<sup>a</sup>, Grégory Abadias<sup>a,\*</sup>

<sup>a</sup> Institut Pprime, Département Physique et Mécanique des Matériaux, UPR 3346, CNRS-Université de Poitiers-ENSMA, SP2MI, Téléport 2, 86962 Futuroscope-Chasseneuil, France

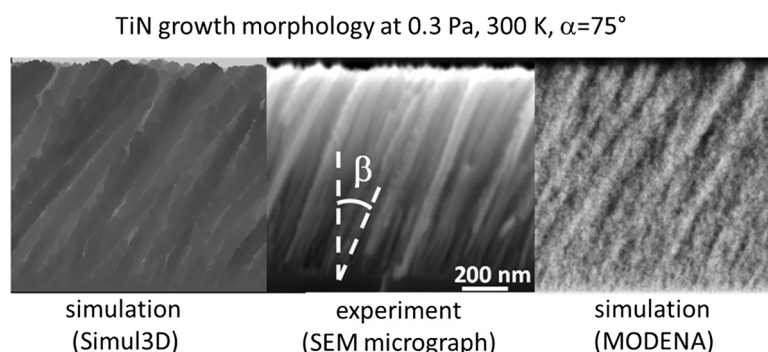
<sup>b</sup> Département de Physique, Unité de Recherche Matériaux, Procédés et Environnement (UR-MPE), Université de Boumerdès, 35000, Algeria

<sup>c</sup> Arts et Métiers ParisTech –LaBoMaP, Rue porte de Paris, 71250 Cluny, France

## HIGHLIGHTS

- Understanding of column development is achieved for TiN films by combining thin film deposition and computational modelling at different pressures
- The particle flux angular distribution reaching the substrate is the key parameter dictating growth morphology and column tilt angle  $\beta$
- TiN columns appear less tilted with increasing pressure for substrate tilt angles  $\alpha \geq 35^\circ$
- Saturation of column tilt angle  $\beta$  around  $25\text{--}30^\circ$  is observed for  $\alpha \geq 65^\circ$  due to the broadening of the angular distribution
- Crossover phenomena of the layer density, surface roughness and resistivity versus angle  $\alpha$  are revealed between 0.3 and 0.5 Pa

## GRAPHICAL ABSTRACT



## ARTICLE INFO

### Article history:

Received 23 July 2018

Received in revised form 7 September 2018

Accepted 10 September 2018

Available online xxxx

### Keywords:

TiN

Reactive magnetron sputtering

Monte Carlo simulations

Particle flux

GLAD

## ABSTRACT

Nanostructured columnar titanium nitride (TiN) thin films were produced by oblique angle deposition using reactive magnetron sputtering. The influence of the angular distribution of the incoming particle flux on the resulting film morphology (column tilt angle, porosity, surface roughness) was studied by varying the inclination angle  $\alpha$  of the substrate at two different working pressures, 0.3 and 0.5 Pa. The microstructural features and columns tilt angles  $\beta_{\text{exp}}$  determined experimentally were compared to those simulated from two kinetic Monte Carlo (KMC) models. With increasing pressure, the TiN columns were found to be less defined but no significant changes in  $\beta_{\text{exp}}$  were revealed. Both KMC models satisfactorily reproduced the experimental findings, the agreement being closer at 0.5 Pa. The evolution of  $\beta$  angle is also discussed with respect to the resulting incidence angle  $\theta_{\text{res}}$  of the incoming flux, this latter quantity accounting for the local incidence angle of individual particles, which may greatly differ from the geometrical angle  $\alpha$ , especially at high working pressure due to the incoming particle – gas collisions. Crossover phenomena between the 0.3 and 0.5 Pa series were revealed from the evolution of the film resistivity, as well as simulated layer density and surface roughness versus  $\alpha$  angle.

## 1. Introduction

Oblique angle deposition (OAD) and glancing angle deposition (GLAD) techniques have emerged as attractive physical vapor deposition routes to synthesize nanostructured and sculptured thin films with dedicated open porosity, large surface area, controlled texture and anisotropic properties [1–5]. By taking advantage of the highly directional vapor flux obtained from thermal or electron-beam evaporation of a solid target in ultra-high vacuum conditions, the production of thin films with well-defined tilted columnar structures is achievable. By employing an additional substrate motion during GLAD, more complex film architectures, like nanorods, zig-zag or spiral structures, can be fabricated [2–4,6–9].

Under stationary mode, films produced under OAD conditions form columns which are oriented towards the incoming vapor flux, making an angle  $\beta$  with the substrate normal [1,2,10]. Experimentally, the columns tilt angle  $\beta$  is ordinarily lower than the angle  $\theta$  formed by the substrate normal and the source direction [1,2,11–13]. The development of such tilted columnar structures is mainly governed by shadowing effect as well as surface diffusion if the experimental conditions allow alleviating from kinetics limitations and ensure sufficient adatom mobility. Although the trend of  $\beta$  increasing monotonically with  $\theta$  was claimed to follow one of the two empirical tangent and cosine rules [14,15], recent experimental works and numerical simulations have shown that the  $\beta$ - $\theta$  relationship is not universal and depends on the material type and growth conditions [11,13,16,17].

It is of prime importance to understand how these columnar structures develop depending on the deposition conditions. Indeed, the columns tilt angle  $\beta$  affects the overall film microstructure (surface roughness, porosity degree) and the resulting optical [9], electrical [18,19] or tribological [20] properties. Such nanostructured thin films find widespread applications in diverse fields, such as gas sensing [7,21], optical devices and photonics [22,23], thermal protective coatings, photovoltaics and fuel cell components, catalysis and electrochemistry, as well as surfaces with controlled wettability [24] and biocompatibility [25]. For most applications implying OAD films, evaporation is the method of choice and has been successfully applied to various materials, including elemental metals and semiconductors (Si, Ge) [26,27], as well as oxide compound films [28,29]. Although less employed for such microstructural design, plasma-based and ion beam-assisted deposition techniques can provide a better control/flexibility in terms of process parameters, offering further routes to tailor the development of columnar structures and expand the panel of their physical characteristics.

While oxide thin films produced at glancing angle incidence have occupied a central position in recent years for their integration as anti-reflective and conductive layers in solar cells, OAD of nitride thin films has been comparatively much less explored. Titanium nitride (TiN) is one of the most well-established engineering materials today that has broad technological applications due to its unique combination of metallic, covalent and ionic bonding character. It has long been employed as a protective, hard and decorative coating [30] but its electronic properties and low thermal conductivity make it also useful as diffusion barriers in microelectronic devices or solar cells [31,32]. Recently, it has emerged as a promising material for plasmonic applications requiring thermal stability (such as photothermal or hot electron devices) due to its high melting point ( $T_m = 3563$  K) combined with high electron conductivity and mobility [33,34]. Therefore, there is a growing interest in synthesizing nanostructured TiN layers, which motivates the implementation of OAD approaches to achieve such goals [35].

Polycrystalline TiN thin films are routinely fabricated by magnetron sputtering (MS) at substrate temperature  $T_s$  in the range of 300–600 K, and working pressure in the 0.2–0.5 Pa range. Such conditions result in a typical columnar growth at normal incidence, corresponding to either 'Zone-I' or 'Zone-T' of structure zone diagrams [36]. However, only few works exist in the literature regarding the growth and properties of TiN films produced by oblique angle MS [37,38].

The particle flux generated from the sputtering of a solid target possesses two main distinctive features with respect to a thermally emitted vapor flux: (1) a much higher kinetic energy of the incoming particles, in the 1–10 eV range and (2) a broader angular distribution due to scattering in the gas phase, as a much higher working pressure, typically in the 0.1–1.0 Pa range, is required to sustain the plasma discharge. The influence of the working gas pressure on the growth morphology of metallic thin films deposited by oblique angle MS has been reported for Ti and Au [4,17,18,39], while the impact of an ionized off-normal flux on the column tilt angle of Cr thin films has been investigated by Elofsson et al. [40] and Greczynski et al. [41] using high power impulse magnetron sputtering discharge. However, to the best of our knowledge, no prior work has been dedicated to investigate the influence of deposition conditions on the column formation and tilt angle of TiN thin films grown by MS at oblique angle incidence.

In this work, we combine an experimental and computational research strategy to systematically study the influence of the angular distribution of the particle flux on the development of columnar TiN thin films. To this end, TiN films were grown by reactive MS at various substrate inclination angles and working pressures, and their microstructural features analyzed by X-ray diffraction, scanning electron microscopy and atomic force microscopy. Experimental data are compared to Monte Carlo (MC) simulation results obtained taking into account the whole deposition process, from ejection of sputtered atoms from the target, transport in the gas phase and three-dimensional (3D) ballistic deposition models.

## 2. Methodology

### 2.1. Thin film deposition

TiN coatings were deposited by direct current reactive MS on (001) Si substrates (size  $2.5\text{ cm} \times 1\text{ cm}$ ) inclined at different tilt angles  $\alpha = 5^\circ, 35^\circ, 65^\circ, 75^\circ$  and  $85^\circ$  with respect to the surface normal of the target (cathode) material. The cathode is a 75 mm diameter disk of pure titanium (purity 99.995%), located at 18 cm from the substrate holder in a confocal configuration, and making a fixed angle of  $25^\circ$  with respect to the vertical axis, see Fig. 1a. The power density on the target was fixed at  $6.8\text{ W}\cdot\text{cm}^{-2}$  and the substrate was polarized by an rf power supply to maintain a constant bias voltage of  $\sim 30\text{ V}$  during deposition. Before the deposition process, the Ti target was sputter-cleaned for 3 min in pure Ar discharge, while the substrate was shielded by a shutter. The inert gas (Ar) and the reactive gas ( $\text{N}_2$ ) were introduced into the chamber through separate mass flow controllers,  $\text{N}_2$  being injected in the vicinity of the substrate using a specific gas ring. Two film series were investigated depending on the total working pressure:  $P = 0.3\text{ Pa}$ , corresponding to 16 sccm of Ar and 0.3 sccm of  $\text{N}_2$ , and  $P = 0.5\text{ Pa}$ , corresponding to 28 sccm of Ar and 0.4 sccm of  $\text{N}_2$ . The  $\text{N}_2$  flow rate was adjusted to obtain stoichiometric TiN films, based on our previous work [42].

All depositions were carried at room temperature (300 K) and in stationary mode, i.e. at fixed azimuthal angle  $\phi$ . To vary the tilt angle  $\alpha$  of the substrate, custom-made individual holders having different inclinations with respect to the main plate holder were used, as schematically shown in Fig. 1a. The zenithal angle  $\alpha$ , defined as the angle between the surface normal to the substrate and the surface normal to the target, is therefore the geometrical angle of the substrate inclination. The case  $\alpha = 0$  corresponds to a substrate surface being parallel to the target surface.

To minimize the effect of the film thickness on the development of columns, the deposition time was adjusted between 83 and 133 min, so as to obtain TiN films with similar layer thicknesses ( $\sim 1\text{ }\mu\text{m}$ ) at different incident angles  $\alpha$ . A reference TiN film, with fully dense microstructure and 1:1 stoichiometry, was also deposited using the following condition:  $P = 0.3\text{ Pa}$ ,  $T = 723\text{ K}$  and  $\alpha = 5^\circ$ .

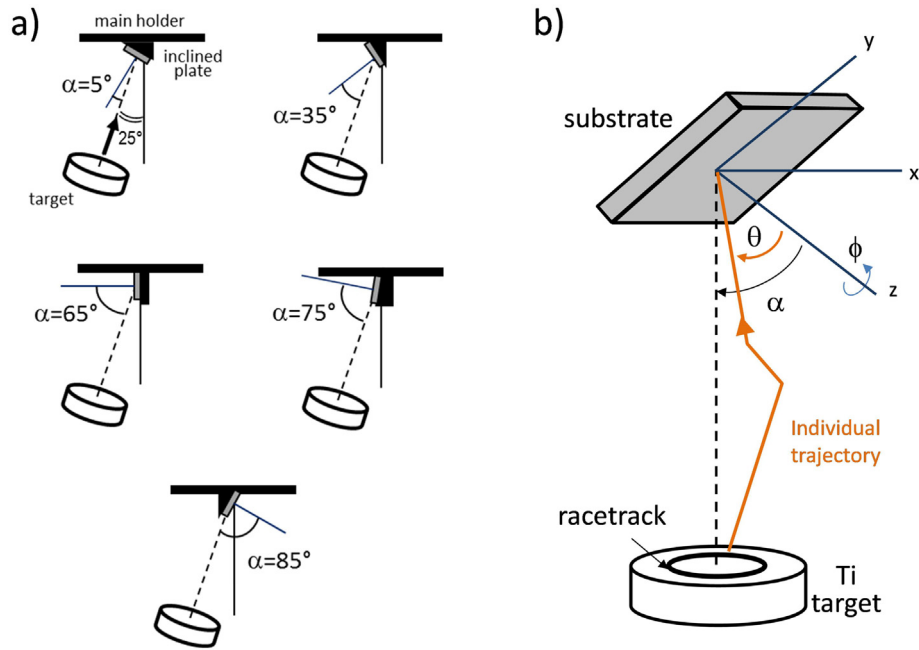


**Fig. 1.** a) Schematic illustration of the substrate holder configurations used to produce TiN thin films at various tilt angles  $\alpha$ . The normal to the target surface (cylindrical cathode) makes an angle of  $25^\circ$  with respect to the vertical axis (solid line). The angle  $\alpha$  is referred with respect to the normal of the substrate surface. b) Schematic showing that the incident angle  $\theta$  of a given particle reaching the substrate may differ from the geometrical tilt angle  $\alpha$  due to collisions during transport in the gas phase.

## 2.2. Microstructural characterization

Cross-section and top-view micrographs of the as-deposited TiN coatings were observed by scanning electron microscopy (SEM) using a field emission gun JEOL 7001F-TTLS microscope operating at 10 and 20 kV, respectively. From the cross-section images, the thickness and the (experimental) column tilt angle  $\beta_{\text{exp}}$  of the TiN films were determined. The deposition rate was calculated from the thickness and deposition time.

The surface roughness was measured for selected samples using a Nanoscope III Multimode atomic force microscope (AFM) from Digital Instrument, operating at ambient air in tapping mode.

The elemental composition of the coatings was determined using wavelength-dispersive X-ray spectroscopy (WDS) unit (Oxford Instruments) attached to the JEOL microscope operating at an accelerating voltage and probe current of 10 kV and 20 nA, respectively. Quantification was performed for nitrogen, oxygen and titanium elements, using the INCA Energy+ software. Overlap between Ti  $L_{\alpha}$  and N  $K_{\alpha}$  lines was accounted for using a correction procedure described elsewhere [43]. Reported atomic fraction values were an average of three measurements.

The crystal structure was examined by X-ray diffraction (XRD) using a Bruker D8 diffractometer operating in Bragg-Brentano  $\theta/2\theta$  configuration using a Cu  $K_{\alpha}$  wavelength (1.5418 Å). XRD patterns were measured along two angular  $2\theta$  ranges, from  $30^\circ$  to  $65^\circ$  and  $72^\circ$  to  $90^\circ$ . These ranges cover the main diffraction lines of TiN, namely 111, 200, 220, 311 and 222, while avoiding the intense 400 Bragg reflection from the single-crystal Si substrate at  $2\theta = 69.13^\circ$ . XRD pole figure measurements were additionally carried out, using a four circle Seifert XRD 3000 diffractometer, to determine the texture of the TiN thin films.

Electrical properties were assessed by standard four-point probe technique. The average value of the electrical resistivity was calculated from measurements taken along two orthogonal in-plane directions of the coating (longitudinal and perpendicular to the projected flux).

## 2.3. Computational simulations

### 2.3.1. Particle flux reaching the substrate: SIMTRA code

The computer code SIMTRA [44] was used to simulate the transport of Ti particle flux from the Ti target towards the substrate. This code provides the angular ( $\theta$ ,  $\Phi$ ) and energy distribution of neutral particles (sputtered Ti atoms and backscattered Ar) reaching the substrate, where  $\theta$  and  $\Phi$  represent the incidence angle and azimuthal angle, respectively. The model assumes binary elastic collisions with neutral gas atoms (Ar) until deposition on a surface occurs. Depending on the Ar working pressure, particles experience a different number of collisional events in the gas phase, which affect both their kinetic energy as well as their trajectories. Therefore, for an individual particle, the (local) incident angle  $\theta$  may differ from the (geometrical) tilt angle  $\alpha$ , as illustrated in Fig. 1b. Such characteristics also depend on the geometry of the vacuum chamber, especially at higher working pressure. Thus, the geometric specification of our chamber was included into the code.

The SIMTRA simulations were carried out using a total of  $10^7$  Ti particles to ensure sufficient statistics of the particles captured by the substrate surface. The nascent angular and energy distributions of Ti sputtered atoms leaving the target were obtained using SRIM calculations [45], assuming the Ti target is bombarded with 350 eV  $\text{Ar}^+$  ions, which corresponds to the plasma discharge characteristics of the present experimental conditions. The racetrack profile used to create the initial position of the particles is of axial symmetry type, fitted to the experimental erosion profile of the Ti target. A Molière screened Coulomb potential was used to describe Ti-Ar interaction. Note that interactions between Ti atoms and  $\text{N}_2$  gas molecules are ignored in the SIMTRA code, but these marginally affect the computed angular distributions since the fraction of  $\text{N}_2$  molecules amounts to  $<2\%$  of the gas mixture under the present experimental deposition conditions. To avoid capturing particles arriving at the back side of the substrate, a cuboid box with dimensions of  $3 \times 3 \times 0.1 \text{ cm}^3$  was used as substrate object. To vary the substrate tilt angle  $\alpha$ , the substrate was rotated around its  $x$  axis, see Fig. 1b.



Other parameters of the simulations, such as the substrate temperature and working pressure, were chosen correspondingly to the experimental conditions: 300 K and  $P = 0.3$  or  $P = 0.5$  Pa, respectively. As a reference for a collision-less transport, SIMTRA calculations were also performed at a fictitious pressure of 0.0 Pa.

### 2.3.2. Kinetic Monte Carlo modeling of thin film growth: Simul3D and MODENA codes

Two independent kinetic Monte Carlo (KMC) models have been used in simulations to grow TiN thin films at various oblique angles. Both are based on a 3D rigid lattice but consider different types of incident particles: either individual Ti and N species, or an ensemble of TiN molecules. Independently of the nature of the particles, the angular distributions of sputtered Ti atoms generated by SIMTRA were used as input parameters in both KMC codes. Note that the energy of the incoming particles is not explicitly taken into account at this stage. Also, the contribution of backscattered Ar was neglected since their fraction is relatively low ( $\sim 2\text{--}3\%$ ) for the case of sputter-deposited TiN films [46] due to similar mass between Ti and Ar species [47].

The first model, implemented in the Simul3D code, uses a simple cubic lattice based on the informatics pixel grid [48]. A cell represents a certain number of atoms and not a single one; in this work a pixel (px) has a dimension of 5 nm, i.e. approximately 12.5 TiN lattice parameters. Say differently, a voxel corresponds to a cubic volume of about  $10^3$  TiN elementary cells. Consequently, surface diffusion could not be taken into account, and this simple model only mimics the growth morphology driven by the incident particle flux. The calculations are here performed at a nano/microscopic scale and allow computing a large number of particles ( $10 \times 10^6$ ) in a very short time. All simulations are performed in a cubic box of  $250 \times 250 \times 200$  px<sup>3</sup>, i.e.  $1.56 \mu\text{m}^3$ . The layer density was calculated from the numbers of pixels filled with a particles normalized to the overall numbers of pixel in the plane.

The second KMC code, named MODENA (MODElling DEposition of Nitride films and their Alloys), has been specifically developed to study the TiN system. Unlike the previous code, individual Ti and N species are taken into account. MODENA employs the superposition of two fcc sub-lattices (metal and nitrogen) to model the cubic rock-salt structure of TiN, with unit cell dimensions equal to half of the TiN bulk lattice parameter, i.e.  $a_0/2 = 0.212$  nm. A complete description of the KMC model can be found elsewhere [49]. In the present work, we apply our model to predict the growth morphologies of TiN films at varying oblique angles and at a fixed substrate temperature of 300 K. Both deposition and diffusion events are considered in the model. However, surface diffusion events were never observed to occur at 300 K, taking into account the relatively large activation barrier of 1.0 eV chosen for both N and Ti diffusing species. For deposition events, the interaction parameter between the incoming particle and the 3D surface was fixed at a distance  $r_0 = \frac{\sqrt{2}}{2}a_0$ . It allows mimicking incoming particles trapping due to short-range interactions with the film surface, similarly to the procedure employed by Alvarez et al. [39]. Both deposition and diffusion events occur on stable sites defined as sites obeying a well-defined surface contact rule, i.e. having a minimum number of nearest ( $N_{nn}$ ) and next-nearest ( $N_{nnn}$ ) neighbours. Here, the surface contact rule is fulfilled when  $N_{nn} \geq 1$  and  $N_{nnn} \geq 3$ . This set of parameters allows reproducing more realistic film properties, as shown in our previous work [49]. All simulations are performed in a cubic box with lateral dimensions equal to 200 unit cells, leading to a simulated volume of  $\sim (42.4)^3 \text{ nm}^3$ .

The simulated column tilt angle,  $\beta$ , is taken as the average of the tilt angle from a sampling of 10 columns and then the error bar corresponds to the root-mean-square value. The analysis was performed in the middle part of the simulated TiN cross-section

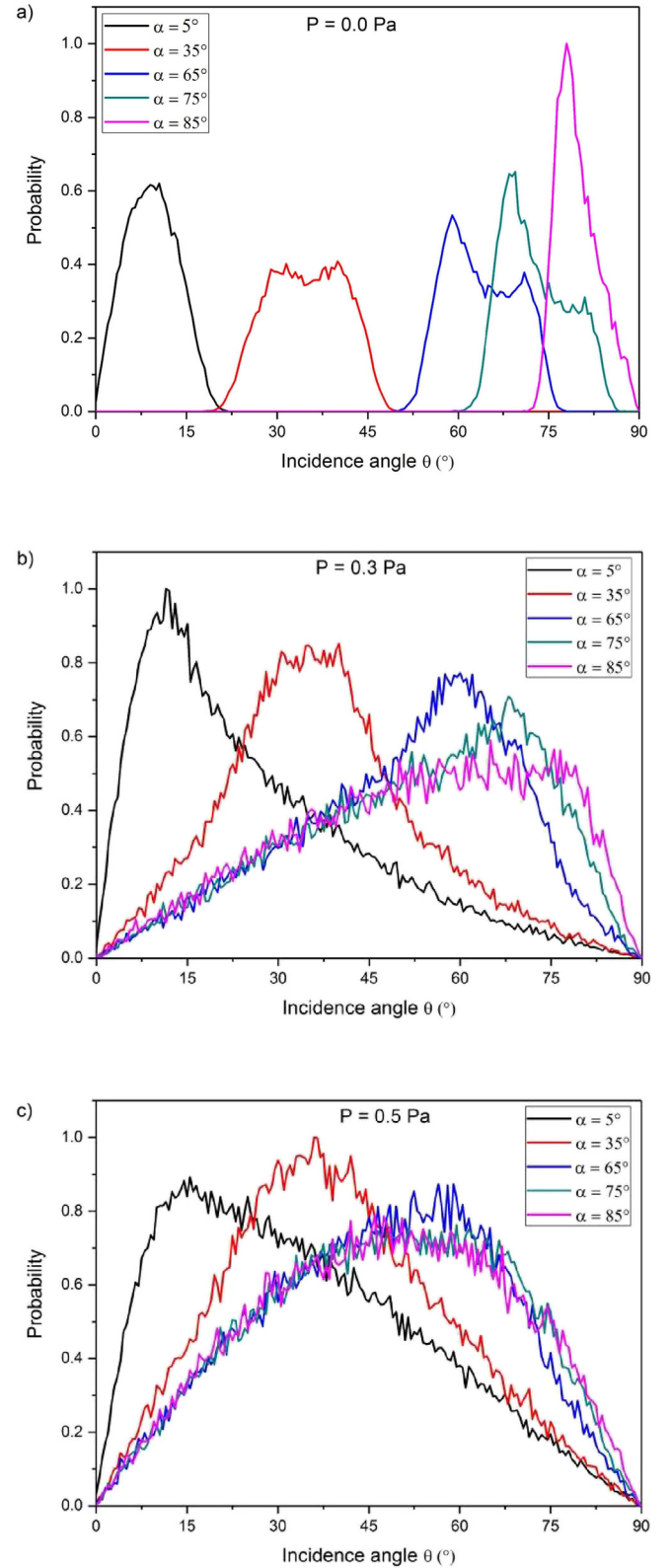


**Fig. 2.** Angular distributions of Ti particles reaching the substrate, as computed from SIMTRA, at three different Ar working pressures: a) 0.0, b) 0.3 and c) 0.5 Pa. Distributions are shown for distinct tilt angles  $\alpha$  of the substrate:  $5^\circ$ ,  $35^\circ$ ,  $65^\circ$ ,  $75^\circ$  and  $85^\circ$ .

images to avoid effects from the substrate interface as well as the influence of column bending at larger film thickness, as also observed experimentally. The density of the simulated TiN films was calculated from the sites occupancy in each layer, and the average

performed throughout the bulk of the film, i.e., excluding the contributions from the substrate interface and film surface (growth front) regions.

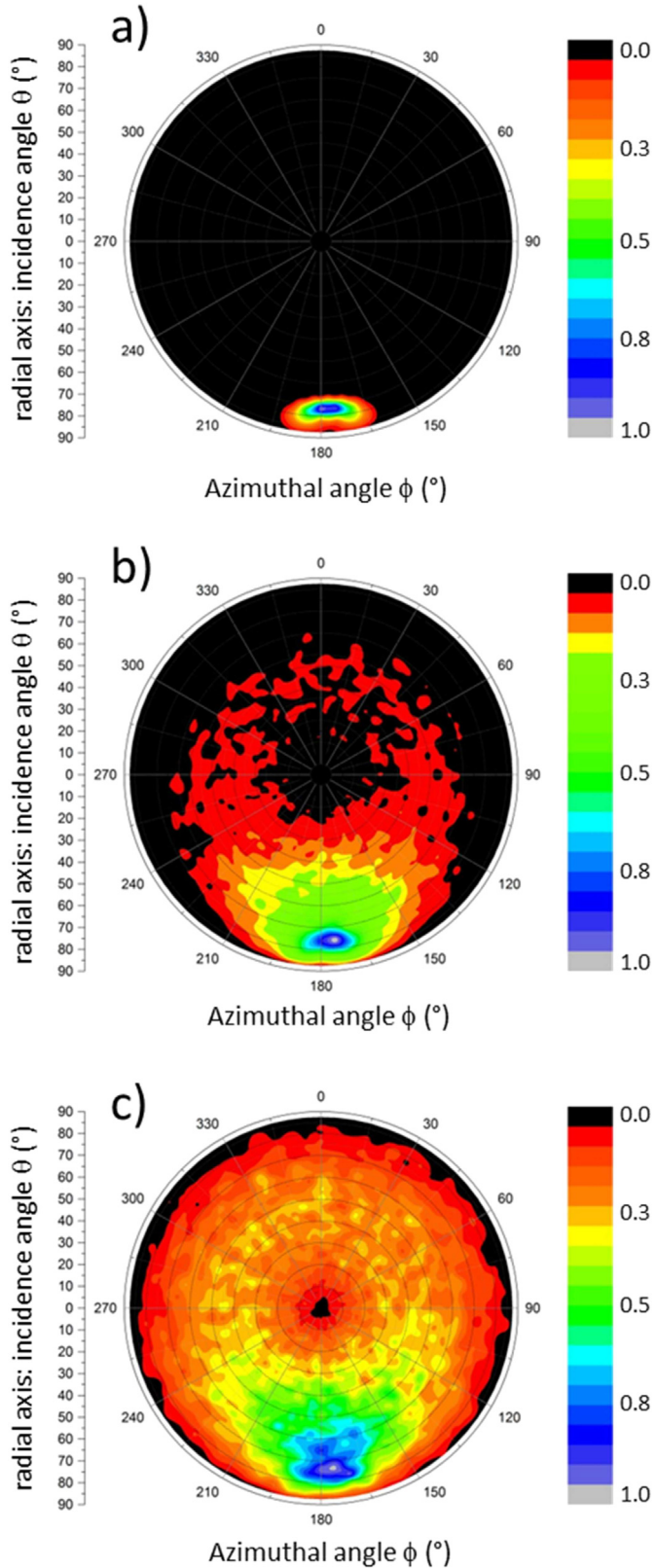


**Fig. 3.** Polar plots of the angular distribution of Ti particles reaching the substrate, as computed from SIMTRA, at three different Ar working pressures: a) 0.0, b) 0.3 and c) 0.5 Pa. The intensity scale is normalized to the maximum probability for each series. Distributions are shown for a substrate tilt angle  $\alpha = 85^\circ$ .

### 3. Results

#### 3.1. Particle flux reaching the substrate

The angular distributions of Ti particles at the substrate position are shown in Fig. 2 for various tilt angles  $\alpha$  of the substrate and at three different pressures  $P = 0.0, 0.3$  and  $0.5$  Pa. A clear angular broadening of the particle flux is observed with increasing pressure. In the absence of collisions ( $P = 0.0$  Pa, Fig. 2a), the particle flux is highly directional, with a mean angular value  $\theta$  corresponding approximately to the geometrical angle  $\alpha$ . However, as the target is not a point source, one can observe a typical distribution width of  $\sim 15$  to  $20^\circ$  (at half maximum). The angular distribution profile becomes asymmetric for  $\alpha \geq 65^\circ$  due to geometrical effects arising from the target race-track. At  $\alpha = 5^\circ$ , the distribution is centered at  $9^\circ$ , which is expected taking into account the finite target size (race-track radius =  $3.5$  cm and target-to-substrate distance =  $18$  cm). At  $P = 0.3$  Pa (Fig. 2b), the shape of the angular distribution changes with increasing  $\alpha$ : it has a large tail extending towards higher (resp. lower) angles at low (resp. high)  $\alpha$  values. One can also notice that at glancing angles,  $\alpha = 75^\circ$  and  $85^\circ$ , the angular distribution is almost the same. This effect is more pronounced at higher pressure,  $P = 0.5$  Pa, see curves obtained at  $\alpha = 65^\circ, 75^\circ$  and  $85^\circ$ . At this pressure, the number of collisions becomes quite significant: Ti particles experience, in average, between 40 and 60 collisions with increasing substrate tilt angle  $\alpha$  (in comparison the number of collision is about 12 to 25 at  $0.3$  Pa, and no collision occurs at  $0.0$  Pa). Therefore, trajectories are much scattered, and particles may impinge on the substrate from a very broad range of incident angles, which explains the results observed in Fig. 2c. It is worth noting that the distributions presented in Fig. 2 are those of the incidence angle  $\theta$  for the computed trajectories of all particles reaching the substrate (for all azimuthal angles corresponding to these trajectories).

To describe more accurately the impinging particles flux, polar plots are shown at different pressures in Fig. 3 for the case  $\alpha = 85^\circ$ . At  $P = 0.0$  Pa, 99.5% of the flux is centered at an incidence angle  $\theta = 76^\circ$  and azimuthal angle  $\phi = 180^\circ$  with little dispersion:  $15^\circ$  in  $\theta$  and  $25^\circ$  in  $\phi$ . This dispersion is purely geometric and comes from the dimension of the race-track, which is clear from the presence of the two lobes. Increasing the pressure leads, as mentioned before, to more scattering events during transport in the gas phase, and consequently to a broader distribution. At  $P = 0.3$  Pa, 45% of the incoming flux is comprised in a small area centered at  $76^\circ$  with few dispersion:  $10^\circ$  in  $\theta$  and  $15^\circ$  in  $\phi$ . The next 40% of the flux takes angles in a large area with  $\theta$  being comprised between  $40^\circ$  and  $90^\circ$  and  $\phi$  between  $140^\circ$  and  $220^\circ$ . The remaining 15% has an incidence angle  $\theta$  mainly around  $40^\circ$ , but the azimuthal angles could take values from  $0^\circ$  to  $360^\circ$ . At  $P = 0.5$  Pa, these three zones are still present but the amount of particles in each ones has changed. The first zone is yet only composed by 25% of the incoming particles, the second zone by the next 35% and the remaining 40% arises from all the space with incidence angles  $\theta$  centered around  $40^\circ$  but with a very broad azimuthal dispersion.

A full description of the angular distribution of the incoming particle flux needs also to account for the azimuthal angle  $\phi$  distribution: it is well known that, whatever the incidence angle  $\theta$  is, opposite azimuthal contributions will result in the development of a vertical column. For

**Table 1**  
Influence of the working pressure  $P$  and substrate tilt angle  $\alpha$  on the resulting incidence angle  $\theta_{\text{res}}$  calculated from individual particle trajectories computed by SIMTRA code.

		Substrate tilt angle $\alpha$				
		$5^\circ$	$35^\circ$	$65^\circ$	$75^\circ$	$85^\circ$
$P$ (Pa)	0.0	$5.0^\circ$	$34.6^\circ$	$63.8^\circ$	$72.9^\circ$	$80.0^\circ$
	0.3	$3.1^\circ$	$24.1^\circ$	$38.1^\circ$	$37.7^\circ$	$32.7^\circ$
	0.5	$2.1^\circ$	$15.4^\circ$	$21.2^\circ$	$19.6^\circ$	$15.6^\circ$



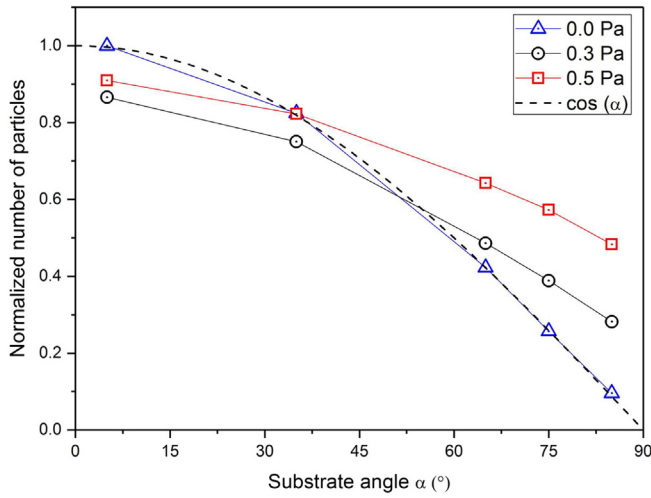


**Fig. 4.** Evolution of the number of Ti particles reaching the substrate with substrate tilt angle  $\alpha$ , at different Ar pressures: 0.0, 0.3 and 0.5 Pa. Values were normalized to the Ti flux obtained at  $\alpha = 5^\circ$  and 0.0 Pa.

this purpose, the *resulting* incidence angle,  $\theta_{\text{res}}$ , has to be introduced in the analysis [16]. This angle represents the average incidence angle taking into account each individual particle with its specific coordinates  $\{\theta, \phi\}$ . The  $[x, y, z]$  direction vectors are summed and normalized and the angles  $\{\theta, \phi\}$  are calculated from this resulting vector. Table 1 lists the  $\theta_{\text{res}}$  values for the three pressures and the different substrate tilt angles  $\alpha$ . In all cases,  $\theta_{\text{res}}$  is smaller than  $\alpha$ . At 0 Pa, the difference remains small, <5%. At 0.3 Pa, the difference is between 30 and 60% and between 50 and 80% at 0.5 Pa. It is worth pointing out that the maximum  $\theta_{\text{res}}$  value is reached at 0.3 and 0.5 Pa for a substrate tilt angle  $\alpha = 65^\circ$ .

The evolution of the normalized number of particles collected at the substrate position is displayed in Fig. 4 as a function of substrate tilt angle  $\alpha$ . As expected for a purely directional flux ( $P = 0.0$  Pa), the evolution follows exactly a cosine law: the projected substrate area on a plane parallel to the target scales with  $\cos \alpha$ . At low substrate tilt angles (below approx.  $30^\circ$ ), and at realistic pressure, scattering in the gas phase induces necessarily less particles on the substrate compared to the case  $P = 0.0$  Pa. Indeed, a fraction of the flux that was impinging the substrate at  $P = 0.0$  Pa is lost on the chamber walls. However, an increase of the pressure from 0.3 to 0.5 Pa leads to more scattering in the gas phase, and in this case to an increase of the number of particles on the substrate. The substrate receives particles that come from all directions

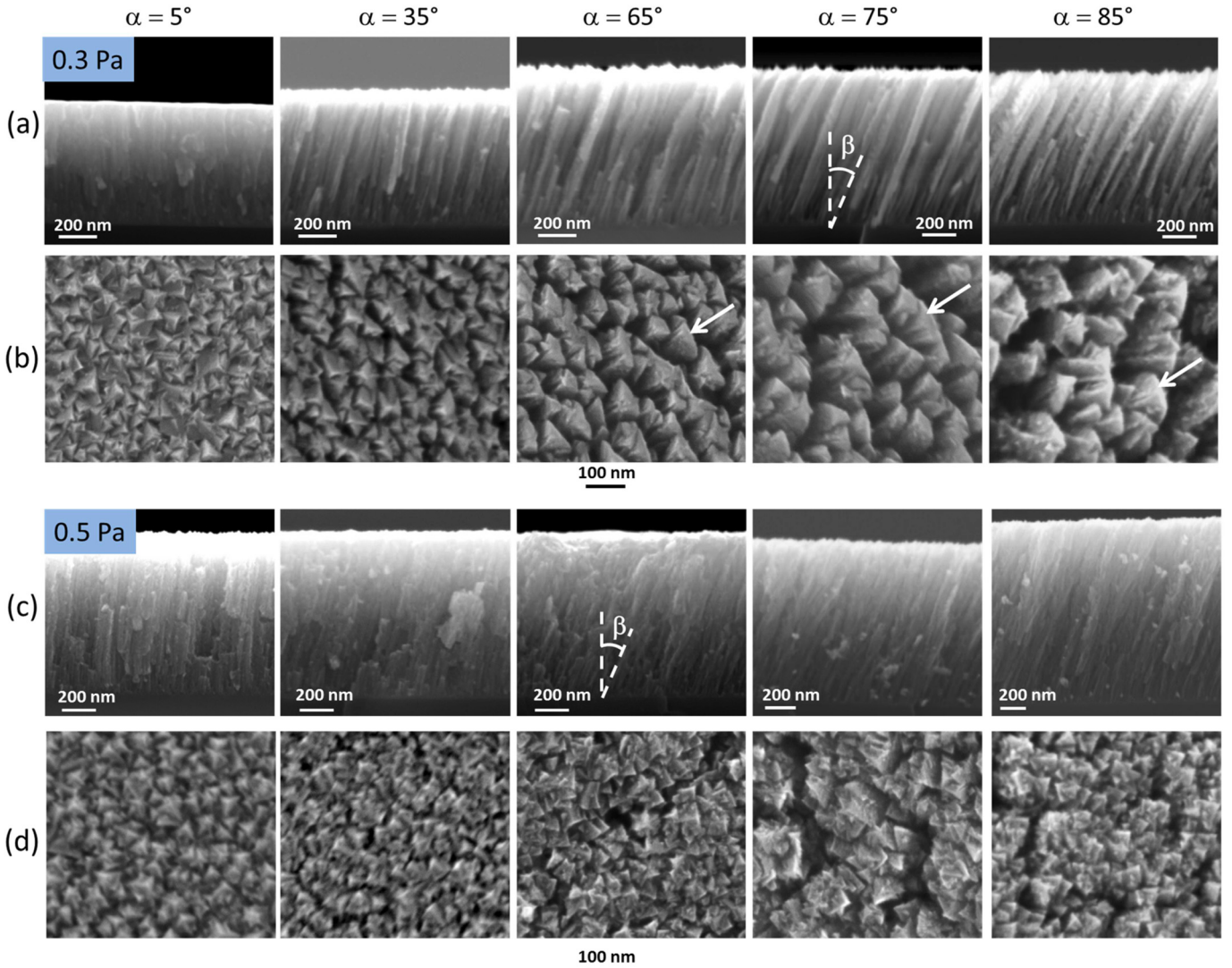


**Fig. 5.** Cross-section (a, c) and plan-view (b, d) SEM images of TiN films deposited at various tilt angles ( $5^\circ$ ,  $35^\circ$ ,  $65^\circ$ ,  $75^\circ$  and  $85^\circ$ ), and two different working pressures: 0.3 Pa (a, b) and 0.5 Pa (c, d). In panel (b), the white arrows indicate the direction of the incident flux. For  $\alpha \geq 65^\circ$ , it is observed that the triangular shaped grains with facets facing the projection flux form the resulting in-plane alignments.



in the azimuthal plane and with lower incidence angle. One can notice that, at high pressure (0.5 Pa), the evolution of the number of particles with the substrate tilt angle is upper the cosine law for  $\alpha > 30^\circ$ . The more the substrate is tilted, the higher the fraction of the flux impinging the substrate at low incidence angle and from all azimuthal directions. Consequently, the number of particles increases and the resulting incident angle  $\theta_{\text{res}}$  decreases (see Table 1).

### 3.2. Growth morphology and microstructural evolution

#### 3.2.1. Experimental results

The growth morphology of TiN films sputter-deposited at 0.3 and 0.5 Pa is shown in Fig. 5a and c, respectively. All films exhibit a well-defined columnar growth, as commonly observed for sputter-deposited TiN films [50]. With increasing substrate tilt angle  $\alpha$ , the inclination of the TiN columns with respect to the substrate normal increases. It is noteworthy that, at 0.3 Pa, the boundaries between columns become more distinctive with increasing substrate tilt angle  $\alpha$ , while at 0.5 Pa the contrast in the cross-sectional SEM micrographs is fuzzier. One can observe that the cleavage occurs at distinct through-thickness locations for the TiN films deposited at 0.5 Pa. At 0.3 Pa, straight columns can be distinguished, extending throughout the entire film thickness, and having a relatively constant diameter, except at  $\alpha = 85^\circ$  where the TiN columns tend to enlarge and bend with increasing film thickness. It is also found that the column density is higher close to the substrate interface.

Insights on the morphological growth development can be gleaned from plane-view SEM micrographs. The surface topography of the films is considerably influenced by the oblique angle deposition and the working pressure. At 0.3 Pa, the column tops emerge at the surface with triangular facets, typical for [111]-textured sputter-deposited TiN films [51]. While these pyramids have a corner pointing upwards for the case  $\alpha = 5^\circ$ , they become tilted with increasing  $\alpha$  values. It is observed that the in-plane arrangement of the columns is such that they have their side facing the projection of the particle flux (indicated by arrows). This is especially visible at  $\alpha = 65^\circ$  and  $75^\circ$ , for which some bundling phenomenon [29] is also noticeable (association of columns in the direction transverse to the incoming flux). At  $\alpha = 85^\circ$ , this in-plane arrangement is less obvious, and the columns tops show manifold facets. Finally, the gap between columns is found to significantly increase with increasing  $\alpha$ , suggesting a higher fraction of inter-columnar porosity. AFM measurements (representative images are shown in Fig. S1 of Supplementary Material file) confirm the existence of coalesced domains at  $\alpha = 65^\circ$ , as well as a drastic increase in the root-mean-square (rms) surface roughness, from 9 to 43 nm, when  $\alpha$  increases from  $5^\circ$  to  $85^\circ$ . This evolution will be further discussed in Section 4 together with the results obtained from KMC simulations.

With increasing pressure, the lateral features decrease in size: compare images shown in Fig. 5b (0.3 Pa) and 5d (0.5 Pa). At 0.5 Pa, if columns with a triangular shape are still visible at  $\alpha = 5^\circ$ , this is no longer the case at higher tilt angles, where the column tops seem to be constituted of many different facets (some having a star-like shape) and exhibit some budding. No specific in-plane alignment of the columns could be revealed at this pressure, see also AFM images of Fig. S1. The surface rms-roughness obtained from AFM imaging for the 0.5 Pa series is lower than at 0.3 Pa, with values ranging from 9 to 19 nm with  $\alpha$  increasing from  $5^\circ$  to  $85^\circ$ .

Fig. 6a shows the evolution of the oxygen content in the TiN films, together with the N/Ti ratio, determined from WDS analysis. The oxygen content in the films is in the 12–28 at.% range. These values are significantly larger compared to the amount (2–3%) found in the reference and fully-dense TiN film deposited at 723 K, suggesting that the presence of oxygen for the OAD TiN film series deposited at 300 K is primarily due to post-growth contamination at ambient air. Indeed, one can observe from Fig. 6a that the oxygen content increases with tilt angle  $\alpha$ , the effect being more pronounced at

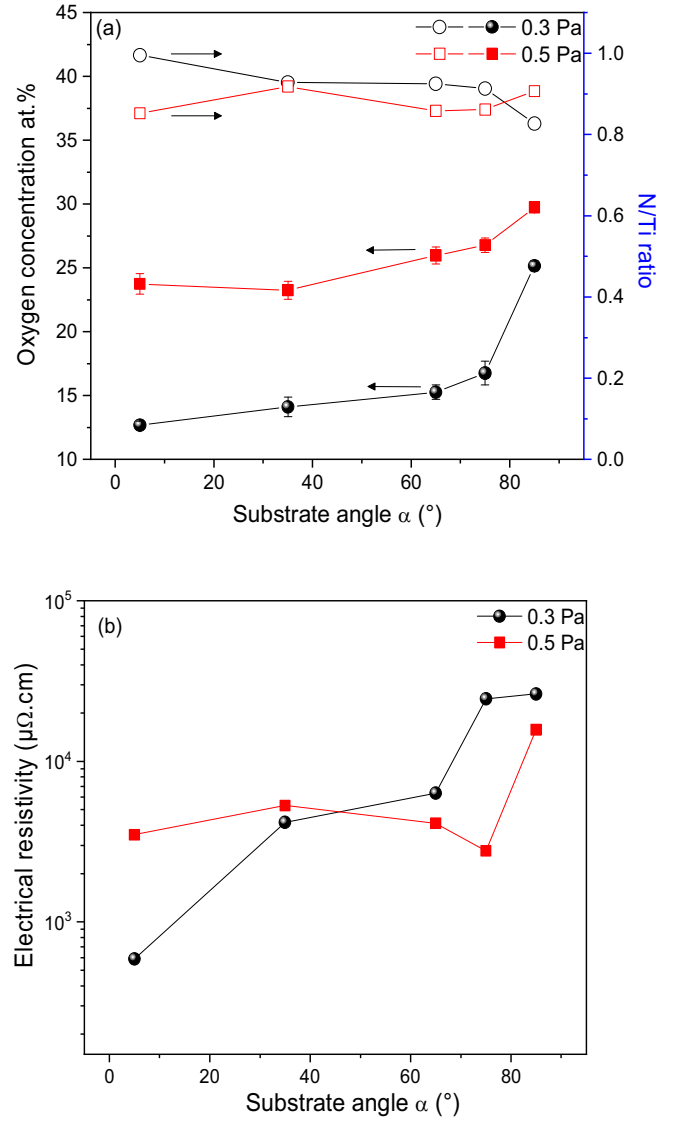
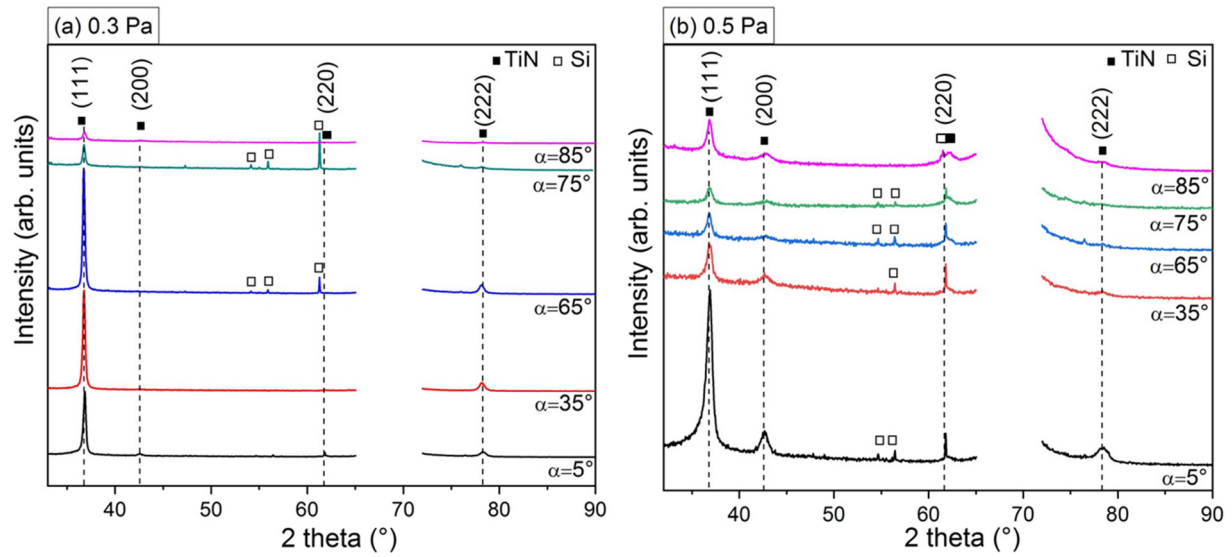


Fig. 6. Evolution with substrate tilt angle  $\alpha$  of (a) oxygen concentration (left axis) and N/Ti ratio (right axis) and (b) electrical resistivity of TiN films sputter-deposited at two different working pressures: 0.3 Pa and 0.5 Pa.

0.3 Pa. A higher degree of oxidation is expected to occur for increasing film porosity. Therefore, the trends depicted in Fig. 6a in terms of oxygen content evolution with  $\alpha$  could bear witness of a higher porosity fraction, and related lower film density, for TiN films deposited at increasing tilt angles. Note that an accurate determination of the film density, e.g. from X-ray reflectivity, is still a challenging issue for films deposited at GLAD conditions. The observation of a sharper increase in the oxygen content at  $\alpha = 85^\circ$  for the 0.3 Pa series sounds in fair agreement with the higher void fraction evidenced from SEM observations (Fig. 5b). TiN films deposited at 0.5 Pa contain systematically higher oxygen content, and the relative increase with  $\alpha$  is less pronounced than for the lower pressure series.

The evolution of N/Ti ratio is rather constant with  $\alpha$  (with a mean value around 0.9), as expected from the constant  $\text{N}_2$  flow supplied during deposition, which corroborates that the observed variations in oxygen content are unlikely attributable to contamination during growth.

These changes in film microstructure and chemical composition with working pressure and substrate tilt angle also manifest themselves by variations in the room temperature electrical resistivity ( $\rho$ ) over several orders of magnitude, see Fig. 6b. Compared to the reference TiN



**Fig. 7.** XRD patterns of TiN films deposited on Si at various tilt angles  $\alpha$  and two different working pressures (a) 0.3 Pa and (b) 0.5 Pa. Parasitic reflections from the Si substrate are marked with empty squares.

film, for which  $\rho = 30 \mu\Omega \cdot \text{cm}$ , the resistivity of the OAD TiN films ranges from  $5.9 \times 10^2$  to  $2.6 \times 10^4 \mu\Omega \cdot \text{cm}$ , indicative of highly-defective films. The  $\rho$  values for the TiN series at 0.3 Pa span a larger range, and a cross-over is observed between the 0.3 and 0.5 Pa series with increasing  $\alpha$ . The higher  $\rho$  values for the 0.5 Pa series for  $\alpha$  below  $40^\circ$  could be ascribed to higher oxygen contamination, while the larger degree of film

porosity at higher  $\alpha$  angles for the 0.3 Pa series could be the dominant contribution to the loss of conductivity for this series.

For both film series, the XRD patterns reported in Fig. 7 show the presence of relatively sharp diffraction lines corresponding to those expected for the cubic (Na-Cl type) structure of TiN. Several reflections, corresponding to (111), (200), (220) and (222) planes, are identified

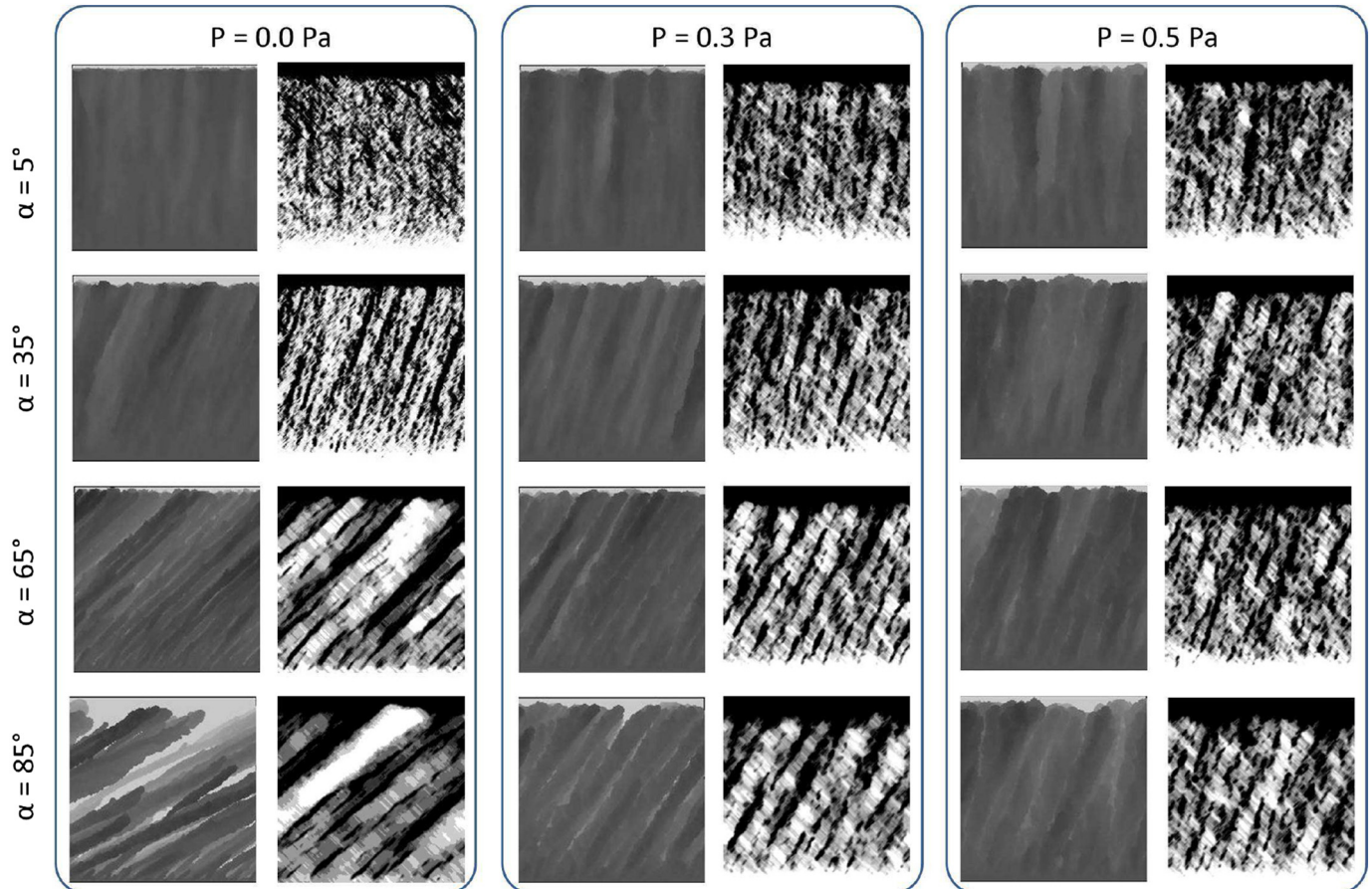


**Fig. 8.** Cross-sectional views (in the yz plane) of the computed TiN growth morphology at different Ar pressures and substrate tilt angles  $\alpha$ . For each pressure, results of Simul3D are shown on the left, while those obtained by MODENA are displayed on the right.

at  $2\theta = 36.8^\circ, 42.5^\circ, 61.8$  and  $78.3^\circ$ , respectively, attesting of the formation of polycrystalline films. However, compared to reference powder diffraction data (ICDD card n°38-1420), the relative intensity of the 111 diffraction line is much higher, suggesting that TiN films develop a [111] preferred orientation. XRD pole figure measurements (not shown here) confirm that the texture is along the [111] direction, but depending on the substrate tilt angle  $\alpha$ , they exhibit either a fiber or a biaxial texture [36]. The biaxial texture, found for the TiN films series at 0.3 Pa and  $\alpha \geq 65^\circ$ , is in line with the SEM observations of Fig. 5b. The correlation between texture evolution and substrate/column tilt angles will be the focus of another work.

Comparing the intensity and width of the XRD lines between both films series, it can be concluded that increasing the working pressure to 0.5 Pa deteriorates the crystalline quality of the films. The larger width is contributed to reduction in grain size and/or increase in microstrain. The higher fraction of oxygen uptake found in these films could also explain the lower diffracted intensity. Finally, no significant shift in the diffraction peak position was observed with varying  $\alpha$  for both films series, suggesting minimal change in the residual stress with  $\alpha$ .

### 3.2.2. Computational results

The cross-section views of the TiN thin film morphologies computed at 0.3 and 0.5 Pa, but also at the fictitious 0.0 Pa, are shown in Fig. 8 using the angular distributions of Fig. 2. For the MODENA code, these angular distributions were used for both N and Ti species. The Simul3D and MODENA simulation boxes are respectively  $200 \text{ px} \times 5 \text{ nm}$  and  $200 \text{ unit cell} \times 0.212 \text{ nm}$ , so their lateral size cannot be directly compared. Note that for better visualization of columns, contrast has been enhanced for images obtained by MODENA (original images showing layer density projection can be found in Fig. S2 of Supplementary material).

Both simulations clearly reproduce a columnar growth, in fairly good agreement with the SEM observations. The nature of the arriving species (individual Ti and N particles in MODENA code and TiN building blocks in Simul3D code) does not seem to significantly alter the results. For the three sets of pressure, there is an increase of the column tilt angle  $\beta$  with increasing substrate tilt angle  $\alpha$ . At fixed  $\alpha$ , the columns appear less tilted with increasing pressure for  $\alpha > 35^\circ$ .

We can also observe at low pressure, i.e., 0.0 Pa and 0.3 Pa, that the columns within the film are qualitatively larger, better defined and the inter-columnar space increases when  $\alpha$  increases. This trend is in line with experimental findings at 0.3 Pa (see Fig. 5a). Straight columns, extending throughout the entire film thickness, and having a relatively constant diameter are visible, except at  $\alpha = 85^\circ$  where the TiN columns tend to enlarge with increasing film thickness. This last trend, columns enlargement with increasing  $\alpha$ , is not observed at 0.5 Pa; moreover, the columns exhibit qualitatively a similar profile from a tilt angle of  $35^\circ$ . Some branching between columns can be observed at this higher pressure. Fig. 8 also reveals that the columns diameter and inter-columnar spacing tend to increase with increasing pressure at low  $\alpha$  angle, i.e. at  $5^\circ$  and  $35^\circ$ . At higher angles, i.e.  $65^\circ$  and  $85^\circ$ , an opposite behavior is observed. Simulated structures also reveal bundling phenomenon of some nano-columns in the transverse direction of the particle flux [29], which is further enhanced at high  $\alpha$  angles.

## 4. Discussion

### 4.1. Influence of working pressure on column tilt angle

The simulated ( $\beta$ ) and experimental ( $\beta_{\text{exp}}$ ) column tilt angles at two different working pressures (0.3 and 0.5 Pa) are plotted against each other in Fig. 9. Both KMC models give, qualitatively, similar trends: i) an increment of the column tilt angle  $\beta$  with respect to the substrate inclination angle, ii) a saturation phenomenon observed at high  $\alpha$  values and iii) lower  $\beta$  values at higher pressure. Computed values reproduce fairly well the experimental evolution, which attests of the reliability of our KMC models. However, it can be noticed that overall simulated  $\beta$  values are

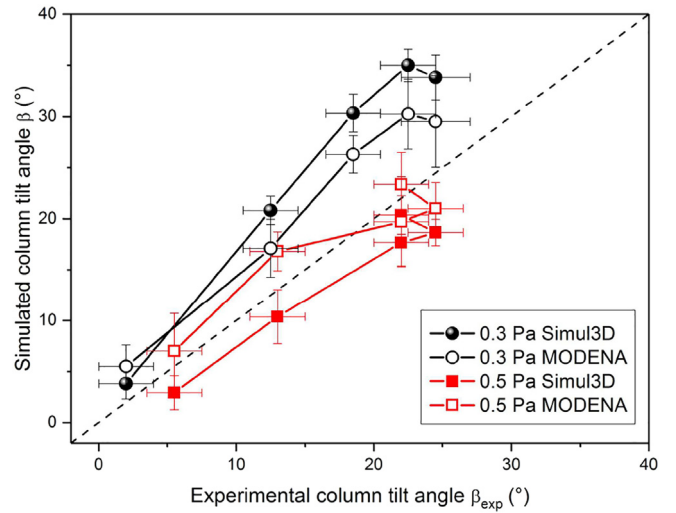


**Fig. 9.** Correlation between simulated ( $\beta$ ) and experimental ( $\beta_{\text{exp}}$ ) column tilt angle at two different working pressures: 0.3 and 0.5 Pa. Filled symbols refer to Simul3D, and empty ones to MODENA.

closer to the experimental values at higher working pressure (0.5 Pa). Because in the simulations, diffusion events are close to zero at the growing temperature of 300 K, the obtained TiN morphologies are essentially dictated by atomic shadowing. This suggests that at 0.5 Pa the final nanostructures are mostly driven by the geometrical flux distribution, while at 0.3 Pa other phenomena occur and influence the growth. This is certainly due to the change in the crystallographic structure and orientation [52] (Fig. 7), which is not taken into account in the simulations. Another contribution which can explain the higher computed  $\beta$  values compared to  $\beta_{\text{exp}}$  at lower pressure is the influence of the deposited energy. As proposed by Alvarez et al. [39], at low pressure, hyperthermal particles will transfer, upon impingement on the surface, part of their kinetic energy and momentum to adatoms, favoring preferential displacement in the forward direction of the vapor flux (biased diffusion). Due to both glancing incidence condition and the appearance of new surfaces (the side of the columns) this additional mechanism affects the otherwise tilted columnar growth, straightening the columns up, and making them cast a larger shadow over the substrate. This mechanism, not yet taken into account in the present simulations, likely explains the overestimation of the column tilt angle at 0.3 Pa compared to  $\beta_{\text{exp}}$  and the increase of the columns diameter and inter-columnar space.

Experimentally, an increase of the pressure from 0.3 Pa to 0.5 Pa does not have a significant influence on the  $\beta_{\text{exp}}$  values. Based on the work of Alvarez et al. on Ti OAD MS films, increasing the working pressure from 0.3 to 0.5 Pa corresponds to an increase of the thermalization degree  $\Xi$  from 0.7 to 1.2, and should result in columns being less inclined at higher pressure [39]. Dervaux et al. [4] reported a monotonous decrease of  $\beta_{\text{exp}}$  from  $52.7^\circ$  to  $13.8^\circ$  in Ti GLAD films ( $\alpha = 85^\circ$ ) with increasing sputtering pressure in the 0.13–1.3 Pa range. Similar trends of decreasing column tilt angle with increasing pressure have been reported for other metallic systems in pure Ar discharge [17,18]. In the case of reactive MS, sputtered metal atoms and nitrogen species may present different angular distributions; especially adsorption of nitrogen can be the result of dissociative adsorption of  $\text{N}_2$  molecule, impingement of  $\text{N}^+$  ions or sputtered N atoms when target is operated under compound mode.

Fig. 10 compares the dependences of the computed column tilt angle  $\beta$  of TiN films on substrate tilt angle  $\alpha$  (Fig. 10a) and on resulting incidence angle  $\theta_{\text{res}}$  (Fig. 10b) at different working pressures: 0.0, 0.3 and 0.5 Pa. In the absence of collisions between particles (at 0 Pa), the evolution of  $\beta$  follows perfectly the tangent rule at low substrate angle ( $\alpha \leq 65^\circ$ ) and the Tait's cosine law at high substrate angle ( $\alpha > 65^\circ$ ). This behavior is commonly reported in the literature [1,2,14,15]. At higher pressure, a deviation from these trends is observed, and the



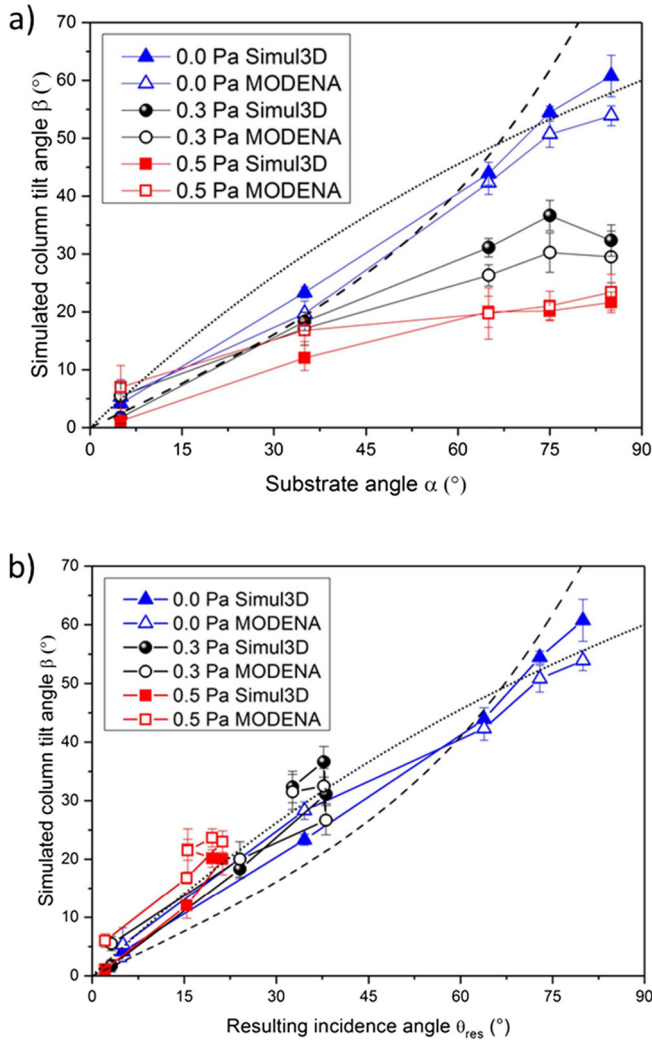
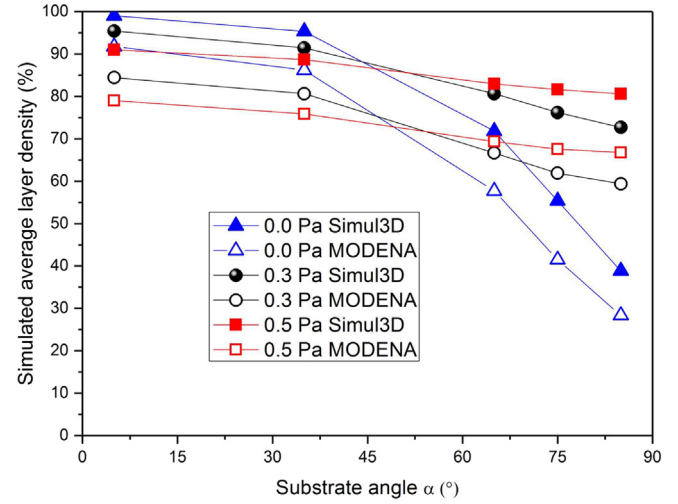


**Fig. 10.** a) Dependence of the computed column tilt angle  $\beta$  of TiN films a) on substrate tilt angle  $\alpha$  and b) resultant incidence angle  $\theta_{res}$  at different working pressures: 0.0, 0.3 and 0.5 Pa. Filled symbols refer to Simul3D, and empty ones to MODENA. The cosine (dotted line) and tangent (dashed line) law-dependences are also indicated.

column tilt angle is found to saturate at high  $\alpha$  angles, as mentioned above. However, if we plot the computed  $\beta$  data versus  $\theta_{res}$ , as introduced in Section 3.1, then an evolution consistent with the two empirical laws is recovered. This indicates that  $\theta_{res}$  is a relevant parameter to describe and predict the columns tilt angle, and points out to the importance of accurately determining the local incidence angle of particle flux reaching the substrate. For evaporation, in the absence of gas scattering and using small-size vapor sources, the assumption  $\alpha = \theta_{res}$  is reasonable, which is no longer the case for MS processes, especially when targets with large dimensions are used as sources and are operated at high working pressure.

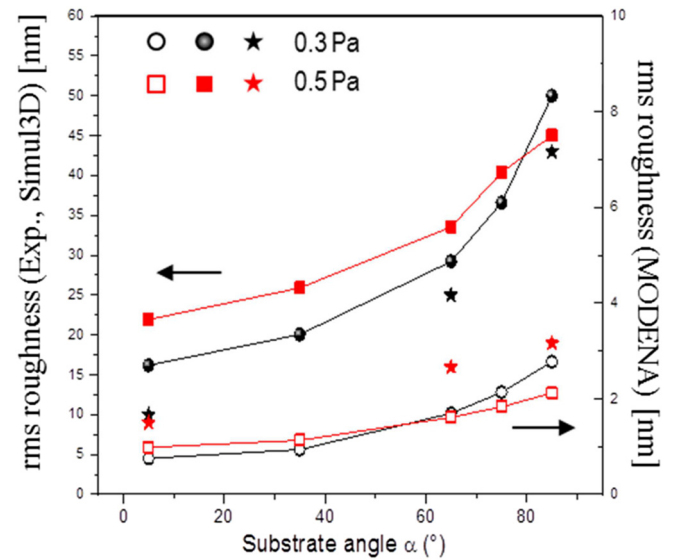
#### 4.2. Influence of working pressure on morphological evolution of deposited structures

Fig. 11 shows the average layer density evolution of the simulated structures with the substrate tilt angle and working pressure. Data extracted from both KMC models display the same trend, even if Simul3D produces in all cases denser films (around 10% more) than MODENA. A decrease of the layer density is observed with the increase of  $\alpha$ , the effect being more pronounced at 0.0 Pa, where film densities as low as 30% are obtained for  $\alpha = 85^\circ$ . This trend is in good agreement with both experimental and computed data reported for Ti MS films grown



**Fig. 11.** Evolution of the simulated average layer density of TiN films with substrate tilt angle  $\alpha$  and working pressure. Filled symbols refer to Simul3D, and empty ones to MODENA.

at 0.15 Pa [39]. Less variations of the layer density vs.  $\alpha$  are found at higher pressures, the lowest values being in the 60–80% range, again in agreement with the data of ref. [39]. This is a direct consequence of the less directional particle flux (see Fig. 2). However, a cross-over phenomenon is observed as a function of substrate tilt angle: at low angles ( $\alpha < 35^\circ$ ), the films at 0.3 Pa are denser than the ones at 0.5 Pa, while at high angles ( $\alpha > 65^\circ$ ), the opposite situation holds. Such crossover was also reflected in the resistivity evolution with  $\alpha$  (see Fig. 6b). Interestingly, it can be noticed that the crossover occurs for the maximum value of the resulting incidence angle  $\theta_{res}$  (see Table 1) meaning there is a critical angle in the interval region  $35^\circ < \alpha < 65^\circ$ , as also revealed for other physical features of OAD metallic films [16]. This crossover could be related to the bundling of nano-columns [29], which is enhanced at higher  $\alpha$  angles due to increased shadow length but also depends on the surface trapping probability (a higher trapping efficiency being favored at higher pressure). The association of columns in the direction transverse to the incoming flux leads to the formation of inter-columnar voids. The larger decrease of the film density at 0.3 Pa is likely



**Fig. 12.** Evolution of the rms-roughness of TiN films with substrate tilt angle  $\alpha$  and working pressure. Filled symbols refer to Simul3D, empty ones to MODENA, and the stars refer to experimental data.



attributed to the larger inter-columnar spacing (see Fig. 8) associated with higher column tilt angles  $\beta$  (see Fig. 10a) and wider coalescing domains along the transverse direction. This is supported by the sharper evolution of the resistivity and oxygen content for  $\alpha > 65^\circ$  (see Fig. 6). At low substrate angle, alteration of the film density is dominated by intra-column vacancies, which in the absence of atom diffusion at 300 K, are formed by shadowing effect.

Fig. 12 plots the simulated and experimental surface rms-roughness for the two working pressures investigated as a function of substrate tilt angle. The simulated roughness is calculated in pxs and then converted in nanometers with the corresponding resolution: 4 nm/px for Simul3D and 0.212 nm/px for MODENA. Experimentally and numerically, the roughness always increases with the substrate tilt angle. Again, a crossover phenomenon between the 0.3 and 0.5 Pa series is observed in the simulations with increasing  $\alpha$ . Experimentally, such crossover is not observed, but there is evidence of a stronger roughness increment with substrate tilt angle at 0.3 Pa compared to the values obtained at 0.5 Pa.

## 5. Conclusions

In this study we have investigated the microstructures of TiN thin films deposited by reactive magnetron sputtering at various oblique incidence angles. The effect of the discharge pressure on the column formation, their inclination with respect to the substrate normal and their surface topography were systematically analyzed and compared to numerical KMC simulations on a 3D rigid lattice and using two different ballistic models. Increasing the substrate tilt angle  $\alpha$  resulted to an increase in the surface roughness and TiN columns tilt angle  $\beta$ . The in-plane arrangement of the columns was affected by the angular distribution of the particle flux, resulting in less tilted TiN columns at higher pressure and to a saturation phenomenon at substrate tilt angles  $\alpha \geq 65^\circ$ .

The increase of the electrical resistivity as a function of the substrate angle  $\alpha$  was attributed to the higher post-growth oxidation of TiN films due to increasing inter-columnar film porosity at high  $\alpha$  angles, this effect being more pronounced at lower pressure. A good agreement between experimental findings and KMC modeling of the TiN film growth by Simul3D and MODENA codes was achieved. Atomistic simulations also revealed crossover phenomena between the 0.3 and 0.5 Pa series from the evolution of the layer density and surface roughness versus  $\alpha$  angle. This opens route to finely tune the physical attributes of nanostructures produced by GLAD techniques by optimization of the working pressure.

## Data availability

The raw/processed data required to reproduce these findings cannot be shared at this time as the data also forms part of an ongoing study.

## Acknowledgements

This work has been performed within the M.ERA-NET project MC<sup>2</sup> “Multi-scale Computational-driven design of novel hard nanostructured Coatings” and funded by the French ANR program (Project No. ANR-13-MERA-0002-02). BB acknowledges the financial support from the Algerian Ministry of Higher Education and Scientific Research through the grant n°173 of the PNE 2016-17 program.

## Appendix A. Supplementary data

Supplementary data to this article can be found online at <https://doi.org/10.1016/j.matdes.2018.09.023>.

## References

- [1] M.M. Hawkeye, M.J. Brett, Glancing angle deposition: fabrication, properties, and applications of micro- and nanostructured thin films, *J. Vac. Sci. Technol. A* 25 (2007) 1317–1335, <https://doi.org/10.1116/1.2764082>.

- [2] A. Barranco, A. Borrás, A.R. Gonzalez-Elipe, A. Palmero, Perspectives on oblique angle deposition of thin films: from fundamentals to devices, *Prog. Mater. Sci.* 76 (2016) 59–153, <https://doi.org/10.1016/j.pmatsci.2015.06.003>.
- [3] D.A. Antartits, R.N. Mott, I. Chasiotis, Silicon nanoprisms fabricated by glancing angle deposition for ultra-compliant films and interfaces, *Mater. Des.* 144 (2018) 182–191, <https://doi.org/10.1016/j.matdes.2018.02.017>.
- [4] J. Dervaux, P.A. Cormier, P. Moskovkin, O. Douheret, S. Konstantinidis, R. Lazzaroni, S. Lucas, R. Snyders, Synthesis of nanostructured Ti thin films by combining glancing angle deposition and magnetron sputtering: a joint experimental and modeling study, *Thin Solid Films* 636 (2017) 644–657, <https://doi.org/10.1016/j.tsf.2017.06.006>.
- [5] S. Sadeghi-Khosravi, K. Robbie, Morphology and crystal texture in tilted columnar micro-structured titanium thin film coatings, *Thin Solid Films* 627 (2017) 69–76, <https://doi.org/10.1016/j.tsf.2017.02.038>.
- [6] Y.G. Yang, D.D. Hass, H.N.G. Wadley, Porosity control in zig-zag vapor-deposited films, *Thin Solid Films* 471 (2005) 1–11, <https://doi.org/10.1016/j.tsf.2004.02.034>.
- [7] X. Xu, M. Arab Pour Yazdi, J.B. Sanchez, A. Billard, F. Berger, N. Martin, Exploiting the dodecane and ozone sensing capabilities of nanostructured tungsten oxide films, *Sensors Actuators B Chem.* 266 (2018) 773–783, <https://doi.org/10.1016/j.snb.2018.03.190>.
- [8] A. Ferreira, J. Borges, C. Lopes, N. Martin, S. Lanceros-Mendez, F. Vaz, Piezoresistive response of nano-architected Ti<sub>2</sub>Cu<sub>3</sub> thin films for sensor applications, *Sensors Actuators A Phys.* 247 (2016) 105–114, <https://doi.org/10.1016/j.sna.2016.05.033>.
- [9] C. Charles, N. Martin, M. Devel, Optical properties of nanostructured WO<sub>3</sub> thin films by Glancing Angle Deposition: comparison between experiment and simulation, *Surf. Coat. Technol.* 276 (2015) 136–140, <https://doi.org/10.1016/j.surfcoat.2015.06.051>.
- [10] A.G. Dirks, H.J. Leamy, Columnar microstructure in vapor-deposited thin films, *Thin Solid Films* 47 (1977) 219–233, [https://doi.org/10.1016/0040-6090\(77\)90037-2](https://doi.org/10.1016/0040-6090(77)90037-2).
- [11] R. Alvarez, C. Lopez-Santos, J. Parra-Barranco, V. Rico, A. Barranco, J. Cotrino, A.R. Gonzalez-Elipe, A. Palmero, Nanocolumnar growth of thin films deposited at oblique angles: beyond the tangent rule, *J. Vac. Sci. Technol., B* 32 (2014), 041802, <https://doi.org/10.1116/1.4882877>.
- [12] B. Tanto, G. Ten Eyck, T.M. Lu, A model for column angle evolution during oblique angle deposition, *J. Appl. Phys.* 108 (2010), 026107, <https://doi.org/10.1063/1.3465296>.
- [13] H. Zhu, W. Cao, G.K. Larsen, R. Toole, Y. Zhao, Tilting angle of nanocolumnar films fabricated by oblique angle deposition, *J. Vac. Sci. Technol. B* 30 (2012), 030606, <https://doi.org/10.1116/1.4710999>.
- [14] J.M. Nieuwenhuizen, H.B. Haanstra, Microfractography of thin films, *Philips Tech. Rev.* 27 (1966) 87–91.
- [15] R. Tait, T. Smy, M. Brett, Modeling and characterization of columnar growth in evaporated-films, *Thin Solid Films* 226 (1993) 196–201, [https://doi.org/10.1016/0040-6090\(93\)90378-3](https://doi.org/10.1016/0040-6090(93)90378-3).
- [16] A. Siad, A. Besnard, C. Nouveau, P. Jacquet, Critical angles in DC magnetron glancing thin films, *Vacuum* 131 (2016) 305–311, <https://doi.org/10.1016/j.vacuum.2016.07.012>.
- [17] J.M. García-Martín, R. Alvarez, P. Romero-Gómez, A. Cebollada, A. Palmero, Tilt angle control of nanocolumns grown by glancing angle sputtering at variable argon pressures, *Appl. Phys. Lett.* 97 (2010), 173103, <https://doi.org/10.1063/1.3506502>.
- [18] P. Pedrosa, A. Ferreira, J.M. Cote, N. Martin, M.A.P. Yazdi, A. Billard, S. Lanceros-Mendez, F. Vaz, Influence of the sputtering pressure on the morphological features and electrical resistivity anisotropy of nanostructured titanium films, *Appl. Surf. Sci.* 420 (2017) 681–690, <https://doi.org/10.1016/j.apsusc.2017.05.175>.
- [19] R. El Beainou, N. Martin, V. Potin, P. Pedrosa, M.A.P. Yazdi, A. Billard, W-Cu sputtered thin films grown at oblique angles from two sources: pressure and shielding effects, *Surf. Coat. Technol.* 343 (2018) 153–159, <https://doi.org/10.1016/j.surfcoat.2017.09.062>.
- [20] P. Stempflié, A. Besnard, N. Martin, A. Domatti, J. Takadom, Accurate control of friction with nanosculptured thin coatings: application to gripping in microscale assembly, *Tribol. Int.* 59 (2013) 67–78, <https://doi.org/10.1016/j.triboint.2012.05.026>.
- [21] A. Singh, A. Sharma, M. Tomar, V. Gupta, Tunable nanostructured columnar growth of SnO<sub>2</sub> for efficient detection of CO gas, *Nanotechnology* 29 (2018), 065502, <https://doi.org/10.1088/1361-6528/aa9bc0>.
- [22] J.Q. Xi, M.F. Schubert, J.K. Kim, E.F. Schubert, M. Chen, S.Y. Lin, W. Liu, J.A. Smart, Optical thin-film materials with low refractive index for broadband elimination of Fresnel reflection, *Nat. Photonics* 1 (2007) 176–179, <https://doi.org/10.1038/nphoton.2007.26>.
- [23] J. Parra-Barranco, M. Oliva-Ramirez, L. Gonzalez-Garcia, M. Alcaire, M. Macias-Montero, A. Borrás, F. Frutos, A.R. Gonzalez-Elipe, A. Barranco, Bending induced self-organized switchable gratings on polymeric substrates, *ACS Appl. Mater. Interfaces* 6 (2014) 11924–11931, <https://doi.org/10.1021/am5037687>.
- [24] P.W. Chi, C.W. Su, D.H. Wei, Control of hydrophobic surface and wetting states in ultra-flat ZnO films by GLAD method, *Appl. Surf. Sci.* 404 (2017) 380–387, <https://doi.org/10.1016/j.apsusc.2017.01.266>.
- [25] U. Allenstein, E.I. Wisotzki, C. Gräfe, J.H. Clement, Y. Liu, J. Schroers, S. G. Mayr, Binary Fe-Pd submicron structures fabricated through glancing angle deposition (GLAD) for bioapplications, *Mater. Des.* 131 (2017) 366–374, <https://doi.org/10.1016/j.matdes.2017.06.032>.
- [26] S. Lucas, P. Moskovkin, Simulation at high temperature of atomic deposition, islands coalescence, Ostwald and inverse Ostwald ripening with a general simple kinetic Monte Carlo code, *Thin Solid Films* 518 (2010) 5355–5361, <https://doi.org/10.1016/j.tsf.2010.04.064>.
- [27] V. Godinho, P. Moskovkin, R. Álvarez, J. Caballero-Hernández, R. Schierholz, B. Bera, J. Demarche, A. Palmero, A. Fernández, S. Lucas, On the formation of the porous structure in nanostructured a-Si coatings deposited by dc magnetron sputtering at oblique angles, *Nanotechnology* 25 (2014), 355705, <https://doi.org/10.1088/0957-4484/25/35/355705>.

- [28] R. Alvarez, L. González-García, P. Romero-Gómez, V. Rico, J. Cotrino, A.R. Gonzalez-Elipe, A. Palmero, Theoretical and experimental characterization of TiO<sub>2</sub> thin films deposited at oblique angles, *J. Phys. D: Appl. Phys.* 44 (2011), 385302. <https://doi.org/10.1088/0022-3727/44/38/385302>.
- [29] C. Lopez-Santos, R. Alvarez, A. Garcia-Valenzuela, V. Rico, M. Loeffler, A.R. Gonzalez-Elipe, A. Palmero, Nanocolumnar association and domain formation in porous thin films grown by evaporation at oblique angles, *Nanotechnology* 27 (2016), 395702. <https://doi.org/10.1088/0957-4484/27/39/395702>.
- [30] J.E. Sundgren, Structure and properties of TiN coatings, *Thin Solid Films* 128 (1985) 21–44.
- [31] A.E. Kaloyeros, E. Eisenbraun, Ultrathin diffusion barriers/liners for gigascale copper metallization, *Annu. Rev. Mater. Sci.* 30 (2000) 363–385.
- [32] B. Shin, Y. Zhu, N.A. Bojarczuk, S. Jay Chey, S. Guha, Control of an interfacial MoSe<sub>2</sub> layer in Cu<sub>2</sub>ZnSnSe<sub>4</sub> thin film solar cells: 8.9% power conversion efficiency with a TiN diffusion barrier, *Appl. Phys. Lett.* 101 (2012), 053903. <https://doi.org/10.1063/1.4740276>.
- [33] P. Patsalas, N. Kalfagiannis, S. Kassavetis, Optical properties and plasmonic performance of titanium nitride, *Materials* 8 (2015) 3128–3154. <https://doi.org/10.3390/ma8063128>.
- [34] P. Patsalas, N. Kalfagiannis, S. Kassavetis, G. Abadias, D.V. Bellas, C. Lekka, E. Lidorikis, Conductive nitrides: growth principles, optical and electronic properties, and their perspectives in photonics and plasmonics, *Mater. Sci. Eng. R. Rep.* 123 (2018) 1–55. <https://doi.org/10.1016/j.mser.2017.11.001>.
- [35] S. Venkataramanababu, G. Nair, P. Deshpande, M.A. Jithin, S. Mohan, A. Ghosh, Chiro-plasmonic refractory metamaterial with Titanium Nitride (TiN) core-shell nanohelices, *Nanotechnology* 29 (2018) 255203.
- [36] S. Mahieu, P. Ghekiere, D. Depla, R. De Gryse, Biaxial alignment in sputter deposited thin films, *Thin Solid Films* 515 (2006) 1229–1249. <https://doi.org/10.1016/j.tsf.2006.06.027>.
- [37] Z. Xie, X. Liu, W. Wang, C. Liu, Z. Li, Z. Zhang, Fabrication of TiN nanostructure as a hydrogen peroxide sensor by oblique angle deposition, *Nanoscale Res. Lett.* 9 (2014) 105. <https://doi.org/10.1186/1556-276X-9-105>.
- [38] Z. Xie, Y.B. Zhang, X.X. Liu, W.P. Wang, P. Zhan, Z.C. Li, Z.J. Zhang, Visible light photoelectrochemical properties of N-doped TiO<sub>2</sub> nanorod arrays from TiN, *J. Nanomater.* 2013 (2013), 930950. <https://doi.org/10.1155/2013/930950>.
- [39] R. Alvarez, J.M. Garcia-Martin, A. Garcia-Valenzuela, M. Macias-Montero, F.J. Ferrer, J. Santiso, V. Rico, J. Cotrino, A.R. Gonzalez-Elipe, A. Palmero, Nanostructured Ti thin films by magnetron sputtering at oblique angles, *J. Phys. D.: Appl. Phys.* 49 (2016), 045303. <https://doi.org/10.1088/0022-3727/49/4/045303>.
- [40] V. Elofsson, D. Magnfalt, M. Samuelsson, K. Sarakinos, Tilt of the columnar microstructure in off-normally deposited thin films using highly ionized vapor fluxes, *J. Appl. Phys.* 113 (2013), 174906. <https://doi.org/10.1063/1.4804066>.
- [41] G. Greczynski, J. Jensen, L. Hultman, Mitigating the geometrical limitations of conventional sputtering by controlling the ion-to-neutral ratio during high power pulsed magnetron sputtering, *Thin Solid Films* 519 (2011) 6354–6361. <https://doi.org/10.1016/j.tsf.2011.04.031>.
- [42] G. Abadias, L.E. Koutsokeras, S.N. Dub, G.N. Tolmachova, A. Debelle, T. Sauvage, P. Villechaise, Reactive magnetron cosputtering of hard and conductive ternary nitride thin films: Ti-Zr-N and Ti-Ta-N, *J. Vac. Sci. Technol. A* 28 (2010) 541–551. <https://doi.org/10.1116/1.3426296>.
- [43] G. Abadias, I.A. Saladukhin, V.V. Uglov, S.V. Zlotski, D. Eyidi, Thermal stability and oxidation behavior of quaternary TiZrAlN magnetron sputtered thin films: influence of the pristine microstructure, *Surf. Coat. Technol.* 237 (2013) 187–195. <https://doi.org/10.1016/j.surfcoat.2013.07.055>.
- [44] K. Van Aeken, S. Mahieu, D. Depla, The metal flux from a rotating cylindrical magnetron: a Monte Carlo simulation, *J. Phys. D.: Appl. Phys.* 41 (2008) 205307.
- [45] J.F. Ziegler, J.P. Biersack, U. Littmark, *The Stopping and Range of Ions in Matter*, Pergamon Press, New York, 1985.
- [46] G. Abadias, L.E. Koutsokeras, A. Sizios, P. Patsalas, Stress, phase stability and oxidation resistance of ternary Ti-Me-N (Me = Zr, Ta) hard coatings, *Thin Solid Films* 538 (2013) 56–70. <https://doi.org/10.1016/j.tsf.2012.10.119>.
- [47] H. Windischmann, Intrinsic stress in sputter-deposited thin films, *Crit. Rev. Solid State Mater. Sci.* 17 (1992) 547–596.
- [48] A. Besnard, N. Martin, L. Carpentier, Three-dimensional growth simulation: a study of substrate oriented films, *IOP Conf. Ser. Mater. Sci. Eng.* 12 (2010), 012011. <https://doi.org/10.1088/1757-899X/12/1/012011>.
- [49] F. Nita, C. Mastail, G. Abadias, Three-dimensional kinetic Monte Carlo simulations of cubic transition metal nitride thin film growth, *Phys. Rev. B* 93 (2016), 064107. <https://doi.org/10.1103/PhysRevB.93.064107>.
- [50] I. Petrov, P.B. Barna, L. Hultman, J.E. Greene, Microstructural evolution during film growth, *J. Vac. Sci. Technol. A* 21 (2003) S117–S128. <https://doi.org/10.1116/1.1601610>.
- [51] S. Mahieu, D. Depla, Reactive sputter deposition of TiN layers: modelling the growth by characterization of particle fluxes towards the substrate, *J. Phys. D.: Appl. Phys.* 42 (2009), 053002. <https://doi.org/10.1088/0022-3727/42/5/053002>.
- [52] D. Depla, A. Besnard, J. Lamas, The influence of the pressure on the microstructure of yttria-stabilized zirconia thin films deposited by dual magnetron sputtering, *Vacuum* 125 (2016) 118–122. <https://doi.org/10.1016/j.vacuum.2015.12.013>.